STUDY ON THE CRYSTALLIZATION OF POLY(ALKYLENE DICARBOXYLATE)S DERIVED FROM 1,9-NONANEDIOL AND MIXTURES WITH DIFFERENT RATIOS OF AZELAIC ACID AND PIMELIC ACID UNITS

A. Díaz, L. Franco, J. Puiggalí*

Departament d'Enginyeria Química, Universitat Politècnica de Catalunya, Av. Diagonal 647, Barcelona E-08028, SPAIN

Correspondence to: **J. Puiggalí (E-mail: Jordi.Puiggali@upc.es)**

ABSTRACT

Polyalkylene dicarboxylates derived from 1,9-nonanediol and mixtures with different ratios of pimelic acid and azelaic acid were synthesized by thermal polycondensation. All samples had a high degree of crystallinity although it was found to decrease with the comonomer content.

Crystallization kinetics of the two homopolymers and the copolymer with the eutectic composition was studied by calorimetric and optical microscopy techniques. Similar Avrami parameters were determined for the three samples and a spherulitic growth with heterogeneous nucleation was deduced. Spherulites showed negative birefringence and a fibrillar or ringed texture depending on the sample. Furthermore, clear differences were found in the primary nucleation density, the spherulitic growth rate and even in the secondary nucleation constant deduced from the Lauritzen-Hoffman treatment.

The three studied samples had a similar arrangement of molecular chains, and consequently their WAXD patterns showed the same strong reflections related to the molecular packing. SAXS data revealed that a lamellar insertion mechanism was characteristic for non-isothermal crystallization from the melt. In addition, significant differences were found between the crystal lamellar thicknesses of the homopolymer and copolymer samples. Diffraction and spectroscopic data suggested that the lamellar crystals of the eutectic copolymer were mainly constituted by azelate units whereas the pimelate units were preferentially located in the amorphous regions including the interlamellar amorphous layer associated with the chain folds.

Keywords: Polyester, copolymers, azelaic acid, pimelic acid, thermal properties, spherulitic growth rate, secondary nucleation, synchrotron radiation.

INTRODUCTION

Great efforts are being focused into the development of biodegradable polymers from renewable resources to avoid problems associated with more conventional petrochemical feedstocks such as decreasing availability, increasing price and indeed environmental pollution caused by plastic waste. Vegetable oils are a promising alternative since coming from abundant and economical biological sources can lead to biodegradable materials. Specifically, potential applications and uses of polyols and polyurethanes derived from plant oils are well known [1-4].

Polyesters also constitute a family of degradable polymers of great and increasing interest since they can cover a wide range of applications as specialities, mainly in the biomedical field, and commodities [5-11]. Poly(alkylene dicarboxylate)s, a specific group within polyesters, are gaining increasing attention because the marketing of polybutylene succinate, which is supplied by Showa High Polymers as Bionolle^{TM} and is characterized by a relatively low production cost, easy processability and good thermal and mechanical properties [12,14]. Several works in the literature deal with the structure and crystallization process of poly(alkylene dicarboxylate)s [15-25]. It was demonstrated that their molecular conformation and packing arrangement depend on the length of the polyalkylene segment and the parity of chemical units involved (i.e. odd or even number of main chain atoms). However, studies have mainly been focused on even-even compounds and little attention has been devoted to the odd-odd series probably because of their expected low thermal properties. This problem can be overcome by using monomers with a high content of methylene groups as the melting point of polyesters generally increases when the ratio between ester and methylene groups in the main chain decreases [26].

Commodity oils like sunflower can provide high purity fatty acids (e.g. oleic acid), which can be used for chemical synthesis of dicarboxylic acid and diol monomers of poly(alkylene dicarboxylate)s. Thus, azelaic acid and 1,9-nonanediol can be obtained by ozonolysis cleavage of the alkene double bond of oleic acid and subsequent oxidation and reduction [3].

The main goal of this work is the basic characterization and study of the crystallization process of odd-odd polyesters derived from natural resources, specifically from 1,9-nonanediol, pimelic and azelaic acids. Special attention is paid to copolymers obtained from mixtures of both dicarboxylic acids since melting points, crystallinities and basic morphologies can vary according to their ratio. Note that azelate and pimelate moeities have a highly similar chemical structure and consequently an identical molecular conformation is expected. In this way, comonomer units could be compatible in such a way that they are able to share a crystalline lattice [27]. This could occur in the isomorphic co-crystallization where only one crystalline phase containing both crystalline units is developed and in the isodimorphic crystallization when at least one of the two crystalline phases incorporates the corresponding minor component in its crystalline lattice. Several works have recently addressed the isomorphic crystallization of copoly(alkylene dicarboxylate)s, which were mainly constituted by even units, such as poly(butylene succinate-*co*-ethylene succinate) [28], poly(butylene succinate-co-propylene succinate) [29], poly(hexamethylene succinate-*co*-hexamethylene adipate) [30], poly(hexamethylene sebacate-*co*-hexamethylene adipate) [31,32], poly(hexamethylene sebacate-*co*-hexamethylene suberate) [33] and poly(hexamethylene suberate-co-hexamethylene adipate) [33]. Results pointed out that isomorphism was feasible and that a smaller difference between the chemical structure of comonomer

units led to less free energy to incorporate foreign units and to a higher extent of comonomer unit inclusion in the host crystalline lattice [33].

EXPERIMENTAL SECTION

Materials

All reagents and solvents were purchased from Sigma-Aldrich and used without further purification.

Poly(nonamethylene pimelate) (PES 9,7), poly(nonamethylene azelate) (PES 9,9), and poly(nonamethylene azelate-*co*-pimelate) (COPES 9,7/9-*x*) were synthesized by thermal polycondensation of the appropriate mixture of dicarboxylic units with an excess of 1,9-nonanediol (2.2:1 molar ratio) (Figure 1). Abbreviations denote PES for polyester, COPES for copolyester, the first digit for the number of carbon atoms of the diol unit, the second digit for the number of carbon atoms of the dicarboxylic unit (or 7/9 for the copolymer) and *x* for the molar ratio between pimelate and azelate units in the reaction mixture. Titanium tetrabutoxyde was used as a catalyst and the reaction was first performed in a nitrogen atmosphere at 150 ºC for 6 h and then in vacuum at 180 ºC for 18 h. Polymers were purified by precipitation with ethanol of chloroform solutions (10 wt-%).

Measurements

Molecular weights were estimated by GPC using a liquid chromatograph (Shimadzu, model LC-8A) equipped with an Empower computer program (Waters) and a refractive index detector. A PL HFIP gel guard precolumn and PL HFIP gel column (Agilent Technologies Deutschland GmbH) were employed. The polymer was dissolved and eluted in 1,1,1,3,3,3-hexafluoroisopropanol at a flow rate of 0.5 mL/min (injected

volume 100 μL, sample concentration 1.5 mg/mL). The number and weight average molecular weights were calculated using polymethyl methacrylate standards

^{1}H- and ^{13}C-NMR spectra were acquired with a Bruker AMX-300 spectrometer operating at 300.1 MHz and 75.7 MHz, respectively. Chemical shifts were calibrated using tetramethylsilane as an internal standard. Deuterated chloroform was used as the solvent.

Infrared absorption spectra were recorded with a Fourier Transform FTIR 4100 Jasco spectrometer in the 4000-600 cm^{-1} range. A Specac model MKII Golden Gate attenuated total reflection (ATR) with a heated Diamond ATR Top-Plate was used.

Calorimetric data were obtained by differential scanning calorimetry with a TA Instruments Q100 series equipped with a refrigerated cooling system (RCS) operating from -90 ºC to 550 ºC. Experiments were conducted under a flow of dry nitrogen with a sample weight of approximately 10 mg while calibration was performed with indium. Heating and cooling runs were performed at rates of 20 ºC/min and 10 ºC/min, respectively.

Spherulites of polyesters were grown from homogeneous melt-crystallized thin films placed between two cover glasses. These films were obtained by evaporation of a dilute solution of the polymer in chloroform. Samples were crystallized isothermally at different temperatures below the melting point using a Linkam temperature control system configured by a THMS 600 heating and freezing stage connected to an LNP 94 liquid nitrogen cooling system. Films with thickness lower than 10 μm were obtained by this experimental procedure. Optical photographs were taken using a Zeiss AxioCam MRC5 digital camera mounted on a Zeiss Axioskop 40 Pol light polarizing microscope. A first-order red tint plate was used to determine the sign of spherulite birefringence under crossed polarizers.

Simultaneous time-resolved SAXS/WAXD experiments were taken at the NCD beamline (BL11) of the Alba synchrotron radiation light facility of Cerdanyola del Valles (Catalunya). The beam was monochromatized to a wavelength of 0.098 nm and the samples were confined between Kapton films. SAXS and WAXD profiles were acquired simultaneously during heating/cooling experiments in time frames of 12 s. Samples were held above fusion for 3 min to erase thermal history before performing the subsequent cooling run. All heating and cooling runs were performed at a rate of 3 ºC/min. Two linear position-sensitive detectors were used [34]: the SAXS detector was calibrated with different orders of diffraction from silver behenate whereas the WAXD detector was calibrated with diffractions of a standard of an alumina (Al_2O_3) sample. The diffraction profiles were normalized to the beam intensity and corrected considering the empty sample background. WAXD peaks were deconvoluted with the PeakFit v4 program by Jandel Scientific Software. The correlation function and corresponding parameters were calculated with the CORFUNC program [35] for Fibre Diffraction / Non-Crystalline Diffraction provided by the Collaborative Computational Project 13.

RESULTS AND DISCUSSION

Synthesis of PES 9,7, PES 9,9 and COPES 9,7/9-*x* samples

The results summarized in Table 1 indicate that samples could be synthesized with a polydispersity index (PDI) and a molecular weight typical of polycondesation reactions involving two monomers with different functionality (i.e. diol and dicarboxylic units). Thus, PDI and M_n ranged from 2.33 to 2.70 and from 7,900 to 13,300 g/mol, respectively. A clear trend for the dependence of molecular weigth with composition was not observed, although lower molecular sizes were achieved when pimelic acid content in the reaction mixture was higher. In any case, molecular weights were

sufficient to ensure film- and fiber-forming properties. Polymerization yields determined after reprecipitation of samples varied in a narrow range (65-78 %); no relationship between yield and monomer feed ratio indicative of a preferred reactivity was observed.

Infrared spectra of all samples synthesized revealed the characteristic absorption bands for methylene (2931-2925 and 2852-2851 cm^{-1}), C=O (1731-1729 cm^{-1}) and C-O (asymmetric and symmetric stretchings at 1242-1223 and 1171-1167 cm^{-1}, respectively). Figure S1a in Supporting information (SI) shows a representative spectrum obtained for PES 9,9 homopolymer whereas a detailed summary of absorption bands is given in Table S1 in SI (discussed below).

^{1}H NMR spectra were highly similar for all samples, showing characteristic signals at 4.04 (O-CH_2), 2.27 (C(O)-CH_2), 1.60 (O-CH_2CH_2 + C(O)-CH_2CH_2) and 1.30 ppm, as can be seen in Figure S2b in SI for PES 9,9. The relative intensity of the last signal was the only difference between the spectra, as logically deduced from the different number of methylene protons of azelate and pimelate units that contributed to the indicated signal.

^{13}C-NMR spectra were more powerful since the vicinal carbons of the dicarboxylate units appeared well differentiated (i.e. 34.29 and 34.10 ppm for azelate and pimelate units, respectively). Figure S2 in SI shows a representative ^{13}C NMR spectrum with the assignment of the observed signals. The variation in intensity associated with the two kinds of C(O)-*C*H_2 carbon atoms with copolymer composition is also pointed out. The areas of these two signals were used to determine the pimelate molar fraction:

$$f_P = A_{34.10} / (A_{34.29} + A_{34.10}) \qquad (1)$$

Table 1 shows that the experimental composition of all copolymers is in full agreement with the feed monomer ratio.

Unfortunately, both ^{1}H and ^{13}C NMR spectra were insensitive to triad effects, and consequently no information concerning sequence distribution could be derived. Specifically, the O-CH_2 protons were not split in the ^{1}H NMR spectra and became insensitive to the two different dicarboxylic units to which the diol could be linked. A triplet was always clearly detected since very few differences were expected due to the large number of aliphatic methylene groups of both azelaic and pimelic units. On the contrary, splitting has been reported when dicarboxylic units of clearly different nature (i.e. aliphatic or aromatic) were used [36].

Infrared spectroscopic data of amorphous and crystalline PES 9,7, PES 9,9 and COPES 9,7/9-0.5 samples

FTIR is highly sensitive to molecular conformation and packing density, hence its usefulness in polymer crystallization studies. Characteristic bands can be correlated to the crystalline and amorphous phases of the bulk, and typically remain distinguishable over the course of crystallization.

FTIR spectra corresponding to semicrystalline and amorphous samples were obtained from the as-synthesized samples at room temperature and at 90 ºC (i.e. about 30 ºC above the melting temperature of each polymer), respectively. Figure 2 compares the characteristic spectra of PES 9,7, PES 9,9 and COPES 9.7/9-0.5 amorphous and semicrystalline samples, whereas the main absorption bands are summarized in Table S1 in SI.

Spectra of amorphous samples were practically identical due to the similar chemical repeat units and also to the similar molecular interactions that should be established in the melt state. Only minor differences were detected in the broad band near 1090-1070 cm^{-1} since it was split in the pimelate rich samples (see asterisk in Figure 2).

Transmission bands generally became broader in the spectra of amorphous samples, and could therefore be distinguished from those associated with crystalline domains, which appeared at the same wavenumber. This is the case, for example, of the asymmetric stretching bands of the C-O group of PES 9,7, which is observed for both crystalline and amorphous phases at 1242 cm^{-1}. On the contrary, a significant wavenumber difference was found for PES 9,9 (i.e. 1240 and 1223 cm^{-1}). In the amorphous state, this stretching mode appeared at the same wavenumber for both homopolymers whereas a large difference was found in the crystalline state due to a different molecular environment of the ester groups. Bands at 1345-1315, 1028-1017, 954-958 and 921-918 cm^{-1} were also noticeable since appeared in the semicrystalline samples only.

The spectrum of the semicrystalline COPES 9,7/9-0.5 sample is highly interesting since some bands were split and appeared at the typical wavenumbers of the corresponding homopolymers. Thus, the asymmetric stretching of the C-O group gave rise to two narrow bands at 1242 and 1224 cm^{-1}, indicating that two kinds of ester groups exist in the copolymer as a result of different interactions with neighboring chains. Specifically, some ester groups had the same arrangement as the PES 9,7 crystalline structure whereas other groups were arranged according to the PES 9,9 structure. Furthermore, it is qualitatively observed that the intensity of the 1224 cm^{-1} band is clearly greater, and consequently the PES 9,9 arrangement seems to be predominant. The difference on intensities cannot be justified by distinct relative absorption coefficients since both bands appeared with similar intensity in the spectra (not shown) of an equimolar mixture of the two homopolymers.

Similar considerations can be made about the copolymer bands at 1344 and 1312 cm^{-1}, which are attributed to deformational CH_2 vibrations of polyesters [37], and are related to those observed at 1345 cm^{-1} and 1315 cm^{-1} in PES 9,7 and PES 9,9 homopolymer

spectra, respectively. Again, the higher intensity was found for the band associated with the PES 9,9 structure. Finally, some bands like that at 1024 cm^{-1} and even that at 956 cm^{-1} appeared in the copolymer at an intermediate wavenumber with respect to the homopolymers (i.e. 1028 and 954, and 1017 and 958 cm^{-1} for PES 9,7 and PES 9,9, respectively).

Calorimetric data of PES 9,7, PES 9,9 and COPES 9,7/9-*x* samples

Thermal properties of the synthesized sample were determined by the four run protocol depicted in Figure 3 for a representative copolymer. Melt and hot crystallization data, together with glass transition temperatures, are summarized in Table S" in SI for all samples. Several points merit further discussion:

a) All samples were semicrystalline and showed a single melting peak independent of the crystallization procedure (i.e. from solution or from the melt). No multiple melting peaks were observed, and consequently no evidence of distinct crystal populations with different lamellar thicknesses was found.

b) Samples were able to crystallize from the melt state at the maximum rate allowed by the equipment. Thus, no cold crystallization peaks were detected in the heating run of quenched samples, whereas melting peaks were clearly observed (e.g. Figure 3d). In addition, these peaks had practically the same enthalpy as those measured at a slow cooling rate for hot crystallized samples (Figure 3b) and even for solution crystallized samples (Figure 3a).

c) The melting temperature of each homopolymer decreased with the comonomer content. The eutectic composition and minimum temperature corresponded to the COPES 9,7/9-50 sample (Figure 4). In addition, PES 9,9 had a higher melting temperature than PES 9,7, as can be presumed from its higher methylene content [26].

d) Melting enthalpies of all samples were always high. Thus, azelate and pimelate units were easily incorporated into the PES 9,7 and PES 9,9 crystalline structures, respectively. Despite the small variation, a slight decrease was observed in the melting enthalpy of each homopolymer when comonomer units were incorporated, as shown in Figure 4 for samples crystallized from the melt. The minimum enthalpy was achieved with the COPES 9,7/9-50 sample and the variation was higher when PES 9,9 was impurified due to its higher enthalpy compared with PES 9,7.

e) Solution crystallized samples always had a higher melting enthalpy than melt crystallized samples. However, a similar dependence of enthalpy upon composition was observed.

f) Non-isothermal crystallization from the melt state required a rather similar degree of supercooling (e.g. between 13 and 18 ºC at a cooling rate of 10 ºC/min) for all samples. Thus, the peak crystallization temperature of PES 9,7 was lower than that of PES 9,9 and logically higher than that of copolymers.

g) Glass transition temperatures ranged in a narrow interval (-45 ºC to -60 ºC) for all samples, the lower values corresponding to COPES 9,7/9-*x* copolymers despite having a higher molecular weight than PES 9,7 homopolymer.

DSC isothermal crystallization study of PES 9,7, PES 9,9 and COPES 9,7/9-0.5 samples

Figure 5a shows the DSC exotherms of the COPES 9,7/9-0.5 sample during crystallization experiments from the melt state at selected temperatures. Peaks logically shifted to higher times and became broader with increasing the crystallization temperature. The time evolution of the relative degree of crystallinity, $\chi(t)$, was determined through the ratio area of the exotherm up to time t divided by the total exotherm area, i.e.:

$$\chi(t) = \int_{t0}^{t} (dH/dt)dt \; / \; \int_{t0}^{\infty} (dH/dt)dt \qquad (2)$$

where dH/dt is the heat flow rate and t_0 the induction time. A characteristic sigmoidal dependence on time was always found, as plotted in Figure 5a (inset).

Kinetic crystallization data were analyzed assuming the well-known Avrami equation [38,39] for primary crystallization:

$$1 - \chi(t) = \exp[-Z\,(t-t_0)^n] \qquad (3)$$

where Z is the temperature-dependent rate constant and n the Avrami exponent whose value varies with the crystallization mechanism. A normalized rate constant, $k = Z^{1/n}$, is usually evaluated for comparison since its dimension (time^{-1}) is independent of the value of the Avrami exponent.

Table 2 summarizes the main kinetic parameters of the primary crystallization process of the homopolymers and COPES 9,7/9-0.5 copolyester, as deduced from the plots of log{-ln[1- $\chi(t)$]} against log (t - t_0) (Figure 7b for COPES 9,7/9-0.5). The values of the Avrami exponent for the hot isothermal crystallizations lie in a narrow range, from 2.25 to 2.94, 2.58 being the average value. This suggests a predetermined (heterogeneous) nucleation with spherical growth that occurred under geometric constraints since the theoretical value should be equal to 3. Sporadic (heterogeneous) and homogeneous nucleation can be clearly discarded as a higher exponent, close to 4, should be derived.

The values of the corresponding reciprocal crystallization half-times ($1/\tau_{1/2}$), calculated as the inverse of the difference between the time at which crystallization begins and the time at which 50% of crystallization is completed, are also summarized in Table 2. This parameter is a direct measure of the crystallization process, and could therefore be used to check the accuracy of the Avrami analysis by comparison with the theoretical kinetic value (i.e., $1/\tau_{1/2} = (Z / \ln 2)^{1/n}$) as reported in Table 2. A similar dependence of $1/\tau_{1/2}$ and the kinetic rate constant on the crystallization temperature for the three polymers can

also be inferred from Figure 5c. This Figure also shows that PES 9,9 crystallized faster than PES 9,7 despite having a greater molecular weight and that the lowest overall crystallization rate corresponded to the copolyester, as could be logically expected. It should be pointed out that the three samples required similar supercooling to start crystallization since the melting points of PES 9,9 and the copolyester samples were the highest and the lowest, respectively.

Isothermal crystallizations of the polymers gave rise to samples characterized by a single melting peak which clearly shifted to higher temperatures with increasing crystallization temperature (e.g. Figure 6a for the COPES 9,7/9-0.5 sample). These results clearly reflect the lamellar thickening effect and make it possible to deduce the equilibrium melting temperatures (i.e. those corresponding to an ideal infinite crystal) by the Hoffman-Weeks approach (Figure 6b) [40]. Theoretical equilibrium melting temperatures of 79.2 and 74.8 ºC were determined for the PES 9,9 and PES 9,7 homopolymers, respectively. Copolymerization decreased these temperatures according to the comonomer content. Thus, the minimum value corresponded to the COPES 9,7/9-0.5 sample (i.e. 72.8 ºC).

Optical microscopy crystallization study of PES 9,7, PES 9,9 and COPES 9,7/9-0.5 samples

All polyester samples crystallized from the melt into spherulites with negative birefringence but different textures (Figures 7a-7c). Ringed spherulites were mainly observed with PES 9,9 over the whole range of tested crystallization temperature whereas fibrillar textures were always observed for PES 9,7. For the sake of completeness, Figure 7d also shows the crystallization of a 50% molar mixture of the two homopolymers, which clearly differentiated from the COPES 9,7/9-0.5 spherulites depicted in Figure 7b. It should be pointed out that both kinds of spherulites (fibrillar

and ringed) were observed in the homopolymer mixture, as expected for an independent crystallization of each polymer. On the contrary, only fibrillar spherulites were observed for the copolymer sample, suggesting that cocrystallization took place, as also deduced from the calorimetric data. It is also worth noting that this copolymer, like PES 9,7, required a high degree of supercooling to crystallize.

Crystallization from the melt of both homopolymers and the representative COPES 9,7/9-0.5 copolymer was studied by optical microscopy in the range where spherulites with adequate dimensions formed and which varied from 62 ºC to 47 ºC depending on the sample. A larger dimension was obtained at temperatures sufficiently high to have a low nucleation rate compared with the crystal growth rate. This size decreased with the crystallization temperature, the minimum temperature considered for each polymer being that corresponding to a final spherulite radius close to 10 μm.

Spherulite radii grew linearly with time up to impingement within the studied temperature intervals (e.g. Figure 8a for the copolymer) and allowed the calculation of the corresponding growth rates, *G*, displayed in Figure 8b. The maximum *G* values measured were clearly different, the highest corresponding to PES 9,9 (i.e. 35 μm/min) and the lowest corresponding to the copolymer (i.e. 6 μm/min), as could be presumed.

Growth data were then analyzed in terms of crystallization regimes by the mathematical expressions derived from the crystal growth and nucleation model proposed by Lauritzen and Hoffman [41]. It is nevertheless true that the physical meaning of this model may be questioned on account of the new theories based on experimental evidences and different theoretical calculations [42,43].

The radial growth rate (*G*) of polymer spherulites was thereby calculated by the Hoffman and Lauritzen equation [41]:

$$G = G_0 \exp[-U^*/(R(T_c - T_\infty))] \exp[-K_g/(T_c (\Delta T) f)] \qquad (4)$$

where G_0 is a constant preexponential factor, U^* represents the activation energy characteristic of the transport of crystallizing segments across the liquid-crystal interface, T_∞ is a hypothetical temperature below which such motion ceases, T_c is the crystallization temperature, R is the gas constant, K_g is the secondary nucleation parameter, ΔT is the degree of supercooling measured as T_m^0-T_c, and f is a correction factor accounting for the variation in the bulk melting enthalpy per unit volume with temperature ($f = 2\,T_c / (T_m^0 + T_c)$).

The sets of parameters most commonly used for U^* and T_∞ are those reported by Williams-Landel-Ferry [44] (WLF) (U^* = 4120 cal/mol and $T_\infty = T_g$ - 51.6 K) and Suzuki and Kovacs [45] (U^* = 1500 cal/mol and $T_\infty = T_g$ - 30 K). The plot of ln G + $U^*/R(T_c\text{-}T_\infty)$ versus 1/(T_c (ΔT) f) for the PES 9,7, PES 9,9 and COPES 9,7/9-0.5 samples fitted well with a linear regression representative of a single crystallization regime (Figure 9) when the second parameter set was employed. The worst regression coefficient was r^2: 0.9934 and the secondary nucleation parameters derived from the slopes of the linear plots of PES 9,7, PES 9,9 and COPES 9,7/9-0.5 crystallization data 9.29 10^4, 1.30 10^5, and 2.15 10^5 K^2, respectively. The highest secondary nucleation constant corresponded to the copolymer, indicating greater difficulty of the lamellar surface in inducing crystallization of incoming polymer chains. Note, also, that the crystal growth rate of COPES 9,7/9-0.5 became strongly dependent on the crystallization temperature, as shown in the G versus temperature plot (Figure 9b). Nucleation constants were similar for the two homopolymers, although a slightly lower value was deduced for PES 9,7.

In addition to the crystal growth rate, the overall crystallization of a sample depends on primary nucleation, which may correspond to heterogeneous nuclei or homogeneous nuclei. Primary nucleation is often a rather complex process as it depends on the

crystallization temperature, density of heterogeneities and presence/absence of nucleating agents. The number of nuclei slightly increased during crystallization, suggesting a thermal nucleation where all nuclei became progressively active for a given crystallization temperature. A slight degree of heterogeneity in the spherulite size was therefore observed at the end of the crystallization process. Figure 9c shows that the nucleation density increased with decreasing the crystallization temperature for the three samples studied and approached a single exponential dependence, which resulted in more active nuclei (i.e. more favorable thermodynamic conditions for nucleus generation) with progressively decreasing the temperature. The lowest density corresponding to the copolymer, as could be presumed from its lower overall crystallization rate determined from calorimetric data. Note also that the copolymer and the PES 9,9 samples had similar molecular weigths (Table 1) and therefore differences on the crystal growth rate and primary nucleation density cannot be attributed to molecular weigth changes. Only PE 9,7 had a slightly lower molecular weight that could justify an increase of both magnitudes. Therefore, the lower values with respect to PE99 cannot be a consequence of he lower molecular size of PE 9,7.

Study on the non-isothermal crystallization of PES 9,7, PES 9,9 and COPES 9,7/9-0.5 samples by time-resolved SAXS/WAXD experiments

Figure 10 contains time-resolved SAXS and WAXD profiles taken during non-isothermal hot crystallization at a cooling rate of 3 ºC/min for a representative polymer (PES 9,7 homopolymer). In all cases, the SAXS long period peak and crystal diffractions appear simultaneously, as expected for a crystallization process controlled by nucleation and crystal growth.

The SAXS long period peak is clearly seen at a value of the scattering vector, $q = 2\pi \sin \theta / \lambda$, in the 0.28-0.39 nm^{-1} range after subtraction of the empty sample background

observed near the beam stop. This peak, which can be attributed to the lamellar structure of the spherulites, appeared at slightly different q values depending on the polymer sample and shifted to higher q values (i.e. lower spacings) during crystallization, showing a more pronounced change in the initial stages.

WAXD profiles showed an amorphous halo (q = 20.3 nm^{-1}) whose intensity decreased with crystallization and on which Bragg reflections formed. The most intense appeared at 0.414-0.413 nm (q = 15.18-15.21 nm^{-1}) and 0.370 nm (q = 16.98 nm^{-1}) and should correspond to the (110) (020) reflections of the typical structure of a polyalkylene dicarboxylate [21-24]. The intensity of the indicated reflections increased sharply at the beginning of crystallization and slowly after a short time interval. This second step corresponds to a secondary crystallization which could also be envisaged from the asymmetric shape of the DSC crystallization peaks (Figure 5b). WAXD profiles of the two homopolymers and the COPES 9,7/9-0.5 copolymer are compared in Figure 13a. Note that the spacings observed for both homopolymers are practically identical and consequently the similar packing arrangement should enable co-crystallization.

The degree of crystallinity of the three samples could be estimated from the corresponding room temperature profiles by considering the intensity of the amorphous background (I_B) and overall intensity (I_T):

$$X_c^{WAX} = (I_T - I_B) / I_T \qquad (5)$$

WAXD measurements indicated that relative crystallinities ranged between 0.68 and 0.48. The highest and lowest values corresponded to PES 9,9 and the copolymer, respectively, in agreement with DSC calorimetric data and the random disposition of dicarboxylic units. It should also be pointed out that PES 9,7 had practically the same crystalline than PES 9,9 (i.e., 0.68 respect to 0.67) as can be qualitatively deduced from the similar amorphous halo observed in the WAXD profile (Figure 11a).

SAXS profiles taken at the end of crystallization revealed clear differences between the lamellar thicknesses of the three samples (Figure 11b), the highest and lowest corresponding to COPES 9,9/7-0.5 and PES 97, respectively. SAXS data were analyzed in more detail during crystallization considering the normalized one-dimensional correlation function [46], $\gamma(r)$, which corresponds to the Fourier transform of the Lorentz-corrected SAXS profile:

$$\gamma(r) = \int_0^\infty q^2 I(q)\cos(qr)dq \;/\; \int_0^\infty q^2 I(q)dq \qquad (6)$$

SAXS data were collected within a limited angular range only. That is why extrapolations to low and high q values were performed using Vonk's model [47] and Porod's law, respectively.

Figure 12a illustrates the correlation functions calculated for the three samples from SAXS profiles taken at the end of crystallization. In general, their analysis allowed the determination of morphologic parameters like: (1) long period, $L_{\gamma,}$ (i.e. r value of the first maximum of the correlation function); (2) amorphous layer thickness, l_a, (i.e. r value for the intersection of the linear regression in the autocorrelation triangle with the ordinate equal to the first minimum of the correlation function); and (3) crystalline lamellar thickness, l_c, (calculated as $L_\gamma - l_a$).

The L_γ values were in all cases close to the long periods determined from twice the value of the first minimum of the correlation function. Thus, the most probable distance between the centers of gravity of two adjacent crystals appeared to be equal to twice the most probable distance between the centers of gravity of a crystal and its adjacent amorphous layer. This suggests a narrow distribution of the layer widths of the major component, which in this case corresponds to the crystal phase.

Data obtained during the non-isothermal hot crystallization revealed a significant decrease of L_γ long spacings at the beginning of the process (i.e. during primary crystallization), although a continuous decrease could still be observed during the secondary crystallization (Figure 12b). These last changes were mainly due to the decrease in the crystalline lamellar thickness, which suggests the occurrence of a lamellar insertion mechanism throughout the crystallization process of the three samples (i.e. formation of thinner lamellar crystals between loosely stacked primary lamellae). Note that the amorphous layer thickness remained practically constant during crystallization.

Figure 12b clearly shows that PES 9,9 had the highest and lowest l_c and l_a values, respectively (i.e. 11.7 and 4.25 nm). Hence, the highest crystallinity within the lamellar stacks, X_c^{SAXS}, (calculated as l_c / L_γ) was determined for PES 9,9 (i.e. 0.74). Crystallinity was clearly lower for PES 9,7 (i.e. 0.60), showing a similar trend to that observed from WAXD crystallinities. Both homopolymers have a similar lamellar thickness but clear differences exist between the crystalline lamellar (i.e. from 11.7 to 9.36 nm) and amorphous layer (i.e. from 4.25 to 6.24 nm) thicknesses. It seems therefore that irregular molecular folds on the lamellar surface should involve larger segments when the polymer is constituted by the slightly more rigid pimelate units.

The greatest amorphous layer thickness (i.e., 7.17 nm) was observed for the copolymer, indicating that chain defects caused by the presence of comonomer units could be placed in the amorphous interlamellar regions. X_c^{SAXS} was minimum for the copolymer (i.e., 0.59), although this crystallinity was very similar to that calculated for PES 9,7 due to the lower crystalline lamellar thickness of the homopolymer having pimelate units.

Results point out that crystallization of COPES 9,7/9-0.5 should start by the arrangement of azelate rich moieties according to the favoured crystallization of PES 9,9 respect to PES 9,7, a feature clearly supported by primary nucleation, crystal growth rate and overall crystallization rate data. Pimelate units seem to be mainly incorporated as defects into the interlamellar amorphous region giving rise to the observed increase in the corresponding spacing. In fact, and as explained above, FTIR spectra revealed also that crystalline bands associated with PES 9,9 were predominant in the copolymer sample.

Combined SAXS and WAXD data were used to verify the assignment of l_a and l_c thicknesses, which could not be distinguished from the analysis of the correlation function [48-51]. Thus, the ratio between X_c^{WAXD} and X_c^{SAXS} is an estimate of the volume-filling fraction of the lamellar stacks, X_S, which should be lower than 1 for a correct assignment. For example, ratios of 0.89, 0.96 and 0.82 were determined for PES 9,9, PES 9,7 and COPES 9,7/9-0.5, respectively, at the end of crystallization.

CONCLUSIONS

Thermal polycondensation using titanium tetrabutoxyde as a catalyst was successfully used to obtain copolyesters constituted by 1,9-nonanediol and different ratios of azelaic and pimelic acid units. Final copolymer compositions were always in good agreement with the feed molar ratio and the attained molecular weights were typical of polycondensation reactions involving monomers with different functionality.

The copolymer with the intermediate composition (i.e. COPES 9,7/9-0.5) had lowest melting temperature and melting enthalpy. However, the crystallinity of this sample was still high. It seemed possible to incorporate comonomer units into the crystalline structure of each homopolymer.

Homopolymers and copolymers crystallized according to a spherulitic growth and a heterogeneous primary nucleation. Significant differences were found between the spherulitic textures (i.e. fibrilar or ringed) and even on the crystallization kinetics of PES 9,7 and PES 9,9 homopolymers. Specifically, non-isothermal crystallization from the melt was less favourable for the PES 9,7 sample and consequently the COPES 9,7/9-0.5 copolymer started to crystallize by the arrangement of azelate moieties.

X-ray diffraction data indicated that crystallization always occurred according to a lamellar insertion mechanism. Significant differences were observed between crystal lamellar and amorphous layer thicknesses of homopolymers and the copolymer with intermediate composition. Optical microscopy, DSC, SAXS and FTIR data suggested that this copolymer crystallized, giving rise to lamellar cores with a predominant PES 9,9 structure, and that pimelate units were mainly located on the amorphous interlamellar regions.

Acknowledgements. Authors are in debt to supports from MINECO and FEDER (MAT2012-36205) and the Generalitat de Catalunya (2009SGR1208). Diffraction experiments were performed at NCD beamline at ALBA Synchrotron with the collaboration of ALBA staff.

REFERENCES

[1] Lligadas G, Ronda JC, Galià M, Cádiz V (2007) Poly(ether urethane) Networks from Renewable Resources as Candidate Biomaterials: Synthesis and Characterization. Biomacromolecules 8:686-692.

[2] Petrovic ZS (2008) Polyurethanes from Vegetable Oils. Polym Rev 48:109-155.

[3] Hojabri L, Kong X, Narine SS (2010) Functional Thermoplastics from Linear Diols and Diisocyanates Produced Entirely from Renewable Lipid Sources. Biomacromolecules 11: 911-918.

[4] Lligadas G, Ronda JC, Galià M, Cádiz V (2010) Plant Oils as Platform Chemicals for Polyurethane Synthesis: Current State-of-the-Art. Biomacromolecules 11:2825-2835.

[5] Doi Y, Steinbüchel A (2002) Polyesters II – properties and chemical synthesis. New York: Wiley-VCH.

[6] Huang SJ (1985) Encyclopedia of polymer science and engineering, vol. 2. New York: Wiley-Interscience, pp 20.

[7] Vert M, Li S M, Spenlehauer G, Guerin P (1992) Bioresorbability and biocompatibility of aliphatic polyesters. J Mater Sci: Mater Med 3:432-446.

[8] Edlund E, Albertsson AC (1999) Novel Drug Delivery Microspheres from Poly(1,5-dioxepan-2-one-co-L-lactide). J Polym Sci Part A: Polym Chem 37:1877-1884.

[9] Kulkarni RK, Moore EG, Hegyeli AF, Leonard F (1971) Biodegradable poly(lactic acid) polymers. J Biomed Mater Res 5:169-181.

[10] Kricheldorf HR, Kreiser-Saunders I, Jürgens C, Wolter D (1996) Polylactides - Synthesis. Characterization and Medical Application. Macromol Symp 103:85-102.

[11] Thombre AG, Cardinal JR (1990) Enciclopedia of Pharmaceutical Technology 2. New York: Marcel Dekker, pp 61.

[12] Fujimaki T (1998) Processability and properties of aliphatic polyesters, 'BIONOLLE', synthesized by polycondensation reaction. Polym Degrad Stab 59:209-214.

[13] Shih Y-F, Wu T-M (2009) Enzymatic degradation kinetics of poly(butylene succinate)nanocomposites. J Polym Res 16:109-115.

[14] Lai SM, Huang CK, Shen HF (2005) Preparation and Properties of Biodegradable Poly(butylene succinate)/Starch Blends. J Appl Polym Sci 97:257-264.

[15] Fuller CS (1939) X-ray investigation of the decamethylene series of polyesters. J Am Chem Soc 61:2575-2580.

[16] Kanamoto T, Tanaka K (1971) Growth and morphology of single crystals of linear aliphatic polyesters. J Polym Sci, Part A-2 9:2043-2060.

[17] Ueda AS, Chatani Y, Tadokoro H (1971) Structural Studies of Polyesters. IV. Molecular and Crystal Structures of Poly(ethylene succinate) and Poly(ethylene oxalate). Polym J 2:387-397.

[18] Aylwin PA, Boyd RH (1984) Aliphatic polyesters as models for relaxation processes in crystalline polymers: 1 Characterization. Polymer 25:323-329.

[19] Liau WB, Boyd RH (1990) Structure and packing in crystalline aliphatic polyesters. Macromolecules 23:1531-1539.

[20] Brandrup J, Immergut H (1989) Polymer Handbook. New York: Wiley.

[21] Almontassir A, Gestí S, Franco L, Puiggalí J (2004) Molecular Packing of Polyesters Derived from 1,4-Butanediol and Even Aliphatic Dicarboxylic Acids. Macromolecules 37:5300-5309.

[22] Gestí S, Almontassir A, Casas MT, Puiggalí J (2004) Molecular packing and crystalline morphologies of biodegradable poly(alkylene dicarboxylate)s derived from 1,6-hexanediol. Polymer 45:8845-8861.

[23] Gestí S, Almontassir A, Casas MT, Puiggalí J (2006) Crystalline Structure of Poly(hexamethylene adipate). Study on the Morphology and the Enzymatic Degradation of Single Crystals. Biomacromolecules 7:799-808.

[24] Gestí S, Casas MT, Puiggalí J (2007) Crystalline structure of poly(hexamethylene succinate) and single crystal degradation studies. Polymer 48:5088-5097.

[25] Lu J-S, Chen M, Lu S-F, Chen C-H (2011) Nonisothermal crystallization kinetics of novel biodegradable poly(butylene succinate-co-2-methyl-1,3-propylene succinate)s. J Polym Res 18:1527-1537.

[26] Champetier G, Monnerie L (1969) Introduction à la chimie macromoléculaire. Paris: Masson et Cie.

[27] Allegra G, Bassi IW(1969) Isomorphism in synthetic macromolecular systems. Adv Polym Sci 6:549-574.

[28] Mochizuki M, Mukai K, Yamada K, Ichise N, Murase S, Iwaya Y (1997) Structural Effects upon Enzymatic Hydrolysis of Poly(butylene succinate-co-ethylene succinate)s. Macromolecules 30:7403-7407.

[29] George Z, Papageorgiou, Bikiaris, Dimitrios N (2007) Synthesis, Cocrystallization, and Enzymatic Degradation of Novel Poly(butylene-co-propylene succinate) Copolymers. Biomacromolecules 8:2437-2449.

[30] Li X, Hong Z, Sun J, Geng Y, Huang Y, An H, et al. (2009) Identifying the Phase Behavior of Biodegradable Poly(hexamethylene succinate-*co*-hexamethylene adipate) Copolymers with FTIR. J Phys Chem 113:2695-2704.

[31] Li X, Sun J, Huang Y, Geng Y, Wang X, Ma Z, et al. (2008) Inducing New Crystal Structures through Random Copolymerization of Biodegradable Aliphatic Polyester. Macromolecules 41:3162-3168.

[32] Liang Z, Pan P, Zhu B, Dong T, Hua L, Inoue Y (2010) Crystalline Phase of Isomorphic Poly(hexamethylene sebacate-co-hexamethylene adipate) Copolyester: Effects of Comonomer Composition and Crystallization Temperature. Macromolecules 43:2925-2932.

[33] Liang Z, Pan P, Zhu B, Inoue Y (2011) Isomorphic crystallization of aliphatic copolyesters derived from 1,6-hexanediol: Effect of the chemical structure of comonomer units on the extent of cocrystallization. Polymer 52:2667-2676.

[34] Rueda DR, García-Gutiérrez MC, Nogales A, Capitán MJ, Ezquerra TA, Labrador A, Fraga E Beltrán D, Juanhuix J, Herranz JF, Bordas J (2006) Versatile wide angle diffraction setup for simultaneous wide and small angle x-ray scattering measurements with synchrotron radiation. Rev Sci Instrum *77*, Art. No. 033904

[35] Rajkumar G, AL-Khayat HA, Eakins F, Knupp C, Squire JM (2007) The CCP13 *FibreFix* program suite: semi-automated analysis of diffraction patterns from non-crystalline materials. J Appl Crystallogr. 40, 178–184.

[36] Herrera R, Franco L, Rodríguez-Galán A, Puiggalí J (2002) Characterization and degradation behavior of poly(butylene adipate-*co*-terephthalate)s. J Polym Sci Part A: Polym Chem 40, 4141-4157.

[37] Pamula E, Blazewicz M, Paluszkiewicz P, Dobrzynski (2001) FTIR study of degradation products of aliphatic polyesters–carbon fibres composites. J Mol Struct 596, 69-75.

[38] Avrami, M (1939) Kinetics of Phase Change. I General Theory. J Chem Phys 7:1103-1120.

[39] Avrami, M (1940) Kinetics of Phase Change. II Transformation-Time Relations for Random Distribution of Nuclei. J Chem Phys 8:212-224.

[40] Hoffman JD, Weeks JJ (1962) Rate of Spherulitic Crystallization with Chain Folds in Polychlorotrifluoroethylene. J Chem Phys 37:1723-1741.

[41] Lauritzen JI, Hoffman JD (1973) Extension of theory of growth of chain-folded polymer crystals to large undercooling. J Appl Phys 44:4340-4352.

[42] Strobl G (2000) From the melt via mesomorphic and granular crystalline layers to lamellar crystallites: A major route followed in polymer crystallization?. Eur Phys J E 3:165-183.

[43] Muthukumar M (2000) Commentary on theories of polymer crystallization. Eur Phys J 3:199-202.

[44] Williams ML, Landel RF, Ferry JD (1955) The Temperature Dependence of Relaxation Mechanisms in Amorphous Polymers and Other Glass-forming Liquids. J Am Chem Soc 77:3701-3707.

[45] Suzuki T, Kovacs A (1970) Temperature dependence of spherulitic growth rate of isotactic polystyrene J. Polym J 1:82-100.

[46] Vonk CG, Kortleve G (1967) X-ray small-angle scattering of bulk polyethylene. Kolloid Z Z Polym 220:19-24.

[47] Vonk CG (1975) A general computer program for the processing of small-angle X-ray scattering data. J Appl Cryst 8:340-341.

[48] Hsiao BS, Gardner KH, Wu DQ, Chu B (1993) Time-resolved X-ray study of poly(aryl ether ether ketone) crystallization and melting behaviour: 1. Crystallization. Polymer 34:3986-3995.

[49] Ikada Y, Jamshida K, Tsuji H, Hyoan SH (1987) Maltopentaose- and maltoheptaose-carrying styrene macromers and their homopolymers. Macromolecules 20:906-908.

[50] Kruger KN, Zachmann HG (1993) Investigation of the melting behavior of poly(aryl ether ketones) by simultaneous measurements of SAXS and WAXS employing synchrotron radiation. Macromolecules 26, 5202-5208.

[51] Hsiao BS, Wang Z, Yeh F, Yan G, Sheth KC (1999) Time-resolved X-ray studies of structure development in poly(butylene terephthalate) during isothermal crystallization. Polymer 40:3515-3523.

FIGURE CAPTIONS

Figure 1. Synthesis of copoly(alkylene dicarboxylate)s from 1,9-nonanediol and pimelic and azelaic acids.

Figure 2. Transmitance FTIR spectra (1400-800 cm^{-1}) of amorphous (red profiles) and semicrystalline (blue profiles) PES 9,7 (a), PES 9,7/9-0.50 (b) and PES 9,9 (c) samples. Boxes highlight characteristic crystalline bands in the spectrum of the copolymer that can be related to each homopolymer (see arrows). Asterisk points to the splitting of the 1090-1070 cm^{-1} amorphous band for the PES 9,7 sample.

Figure 3. DSC traces obtained with the COPES 9,7/9-0.50 copolymer during the heating run (20 ºC/min) of the as-synthesized sample (a), the cooling run (10 ºC/min) after keeping the sample in the melt state for three minutes (b), the heating run (20 ºC/min) of the hot crystallized sample (c) and the heating run (20 ºC/min) of a sample previously cooled at the maximum rate allowed by the equipment from the melt state (d). The inset shows a magnification where the glass transition is clearly observed.

Figure 4. Variation of the melting temperature and enthalpy of poly(nonamethylene azelate-*co*-pimelate)s with the molar percentage of azelate units. Enthalpies are given as kJ/mol considering the molecular weight of the repeat unit determined according to the copolymer composition.

Figure 5. a) Exothermic DSC peaks corresponding to the hot isothermal crystallizations of COPES 9,7/9-0.50 at temperatures between 54 and 51 ºC. Inset shows the development of relative crystallinity over time for the indicated isothermal crystallizations. b) Avrami plots corresponding to the isothermal crystallization of

COPES 9,7/9-0.50. c) Overall crystallization rates (full symbols and solid lines) and the reciprocal of the crystallization half-times (empty symbols and dashed lines) determined at different temperatures for PES 9,9 (○), PES 9,7 (Δ) and COPES 9,7/9-0.50 (□) samples.

Figure 6. a) DSC heating runs (20 ºC/min) of COPES 9,7/9-0.50 samples isothermally crystallized at temperatures ranging from 54 to 51 ºC. b) Hoffman-Weeks plot of temperatures corresponding to endothermic melting peaks versus crystallization temperature for several COPES 9,7/9-*x* samples. For the sake of clarity experimental data of some intermediate compositions are described by dashed lines. Equilibrium melting temperatures are explicitly indicated at the corresponding intersection points.

Figure 7. Polarized optical micrographs of spherulites of PES 9,7 (a), COPES 9,7/9-0.50 (b) and PES 9,9 (c) crystallized at temperatures of 53 ºC, 51 ºC and 59 ºC, respectively. For the sake of completeness, spherulites of a 50% molar mixture of PES 9,7 and PES 9,9 homopolymers and crystallized at 56 ºC are shown in (d).

Figure 8. a) Plots of COPES 9,7/9-0.50 spherulite radii versus crystallization time for isothermal hot crystallizations performed at temperatures between 50.6 and 53 ºC. b) Temperature dependence of the crystal growth rate for PES 9,9, PES 9,7 and COPES 9,7/9-0.50 samples. c) Change in the nucleation density of PES 9,9, PES 9,7 and COPES 9,7/9-0.50 samples with isothermal crystallization temperature.

Figure 9. Plot of $\ln G + U^* / R(T_c - T_\infty)$ versus $1 / T_c (\Delta T) f$ to determine the K_g nucleation parameter of PES 9,9, PES 9,7 and COPES 9,7/9-0.50 samples.

Figure 10. Time-resolved SAXS (a) and WAXD (b) three-dimensional profiles of PES 9,7 during non-isothermal hot crystallization at 3 ºC/min.

Figure 11. WAXD (a) and SAXS (b) profiles of PES 9,9, PES 9,7 and COPES 9,7/9-0.50 samples taken at room temperature. The amorphous halo obtained by deconvolution is explicitly shown for the copolymer sample.

Figure 12. Correlation functions (a) for non-isothermal hot crystallization of PES 9,9, PES 9,7 and COPES 9,7/9-0.50 samples. b) Temperature evolution of L_γ (♦), l_c (▲), and l_a (■) during non-isothermal hot crystallization performed at 3 ºC/min with PES 9,9 (dashed lines), PES 9,7 (solid lines) and COPES 9,7/9-0.50 (dotted lines) samples.

Table 1. Synthesis data of studied polyesters.

Polymer	Yield (%)	f_P[a]	M_n[b] (g/mol)	M_w[b] (g/mol)	PDI[b,c]
PES 9,7	73	1	7,900	19,600	2.47
COPES 9,7/9-0.85	67	0.86	9,400	21,900	2.33
COPES 9,7/9-0.70	76	0.71	9,800	23,000	2.36
COPES 9,7/9-0.50	78	0.53	13,500	32,300	2.40
COPES 9,7/9-0.30	78	0.32	11,700	29,900	2.57
COPES 9,7/9-0.15	65	0.17	12,700	31,800	2.50
PES 9,9	73	0	13,300	35,900	2.70

[a]Pimelate molar fraction determined from ^{13}C NMR spectra.
[b]From GPC.
[c]Polydispersity index.

Table 2. Main crystallization kinetic parameters determined by DSC for the two homopolymers and the copolymer with the highest comonomer content.

Sample	T (ºC)	$Z \cdot 10^6$ (s^{-n})	n	$K \cdot 10^3$ (s^{-1})	$1\ \tau_{1/2} \cdot 10^3$ (s^{-1})	$(Z/\ln 2)^{1/n} \cdot 10^3$ (s^{-1})
PES 9,7						
	52	8.49	2.39	7.54	8.87	8.79
	53	0.34	2.66	3.71	4.30	4.26
	54	0.26	2.47	2.19	2.56	2.55
	55	0.063	2.48	1.27	1.48	1.48
	56	$2.21\ 10^{-03}$	2.63	0.51	0.58	0.58
	57	$8.55\ 10^{-05}$	2.88	0.32	0.35	0.35
COPES 9,7/9-0.50						
	51	8.15	2.26	5.58	6.59	6.56
	52	2.99	2.25	3.53	4.15	4.15
	52.5	0.13	2.51	1.79	2.09	2.08
	53	0.025	2.51	0.94	1.10	1.09
	54	$1.78\ 10^{-04}$	2.78	0.31	0.36	0.36
PES 9,9						
	56	18.48	2.60	15.23	17.93	17.5
	57	0.28	2.94	5.89	6.82	6.67
	58	0.077	2.81	2.92	3.31	3.32
	59	$2.80\ 10^{-03}$	2.79	0.86	0.97	0.99

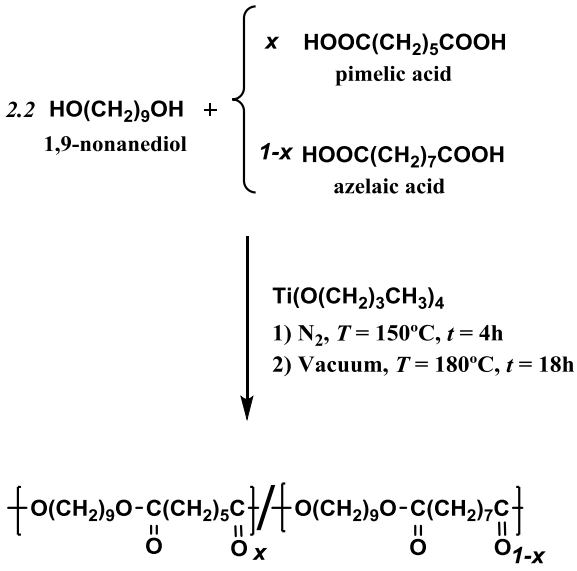

COPES 9,7/9 -x

FIGURE 1

Díaz *et al.*

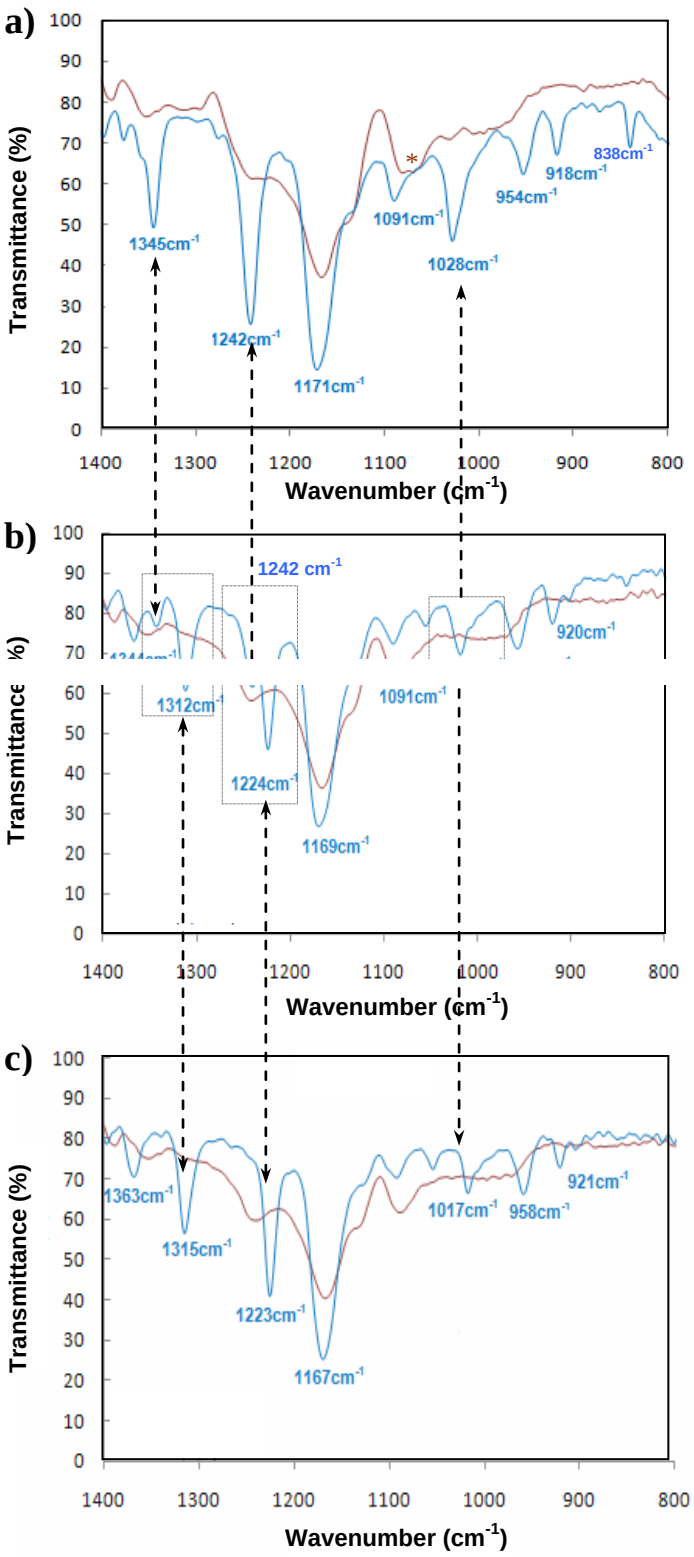

FIGURE 2

Díaz *et al.*

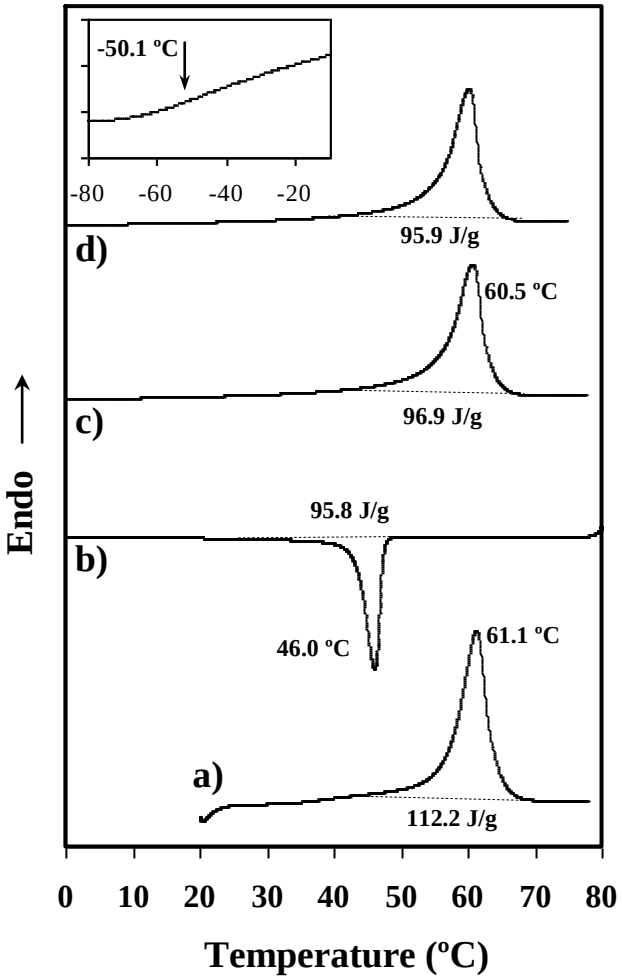

FIGURE 3

Díaz *et al.*

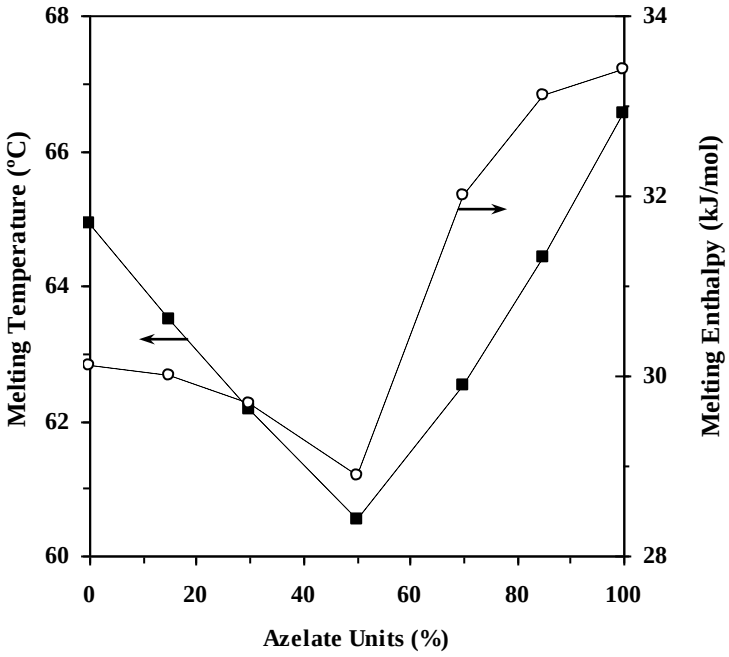

FIGURE 4

Díaz *et al.*

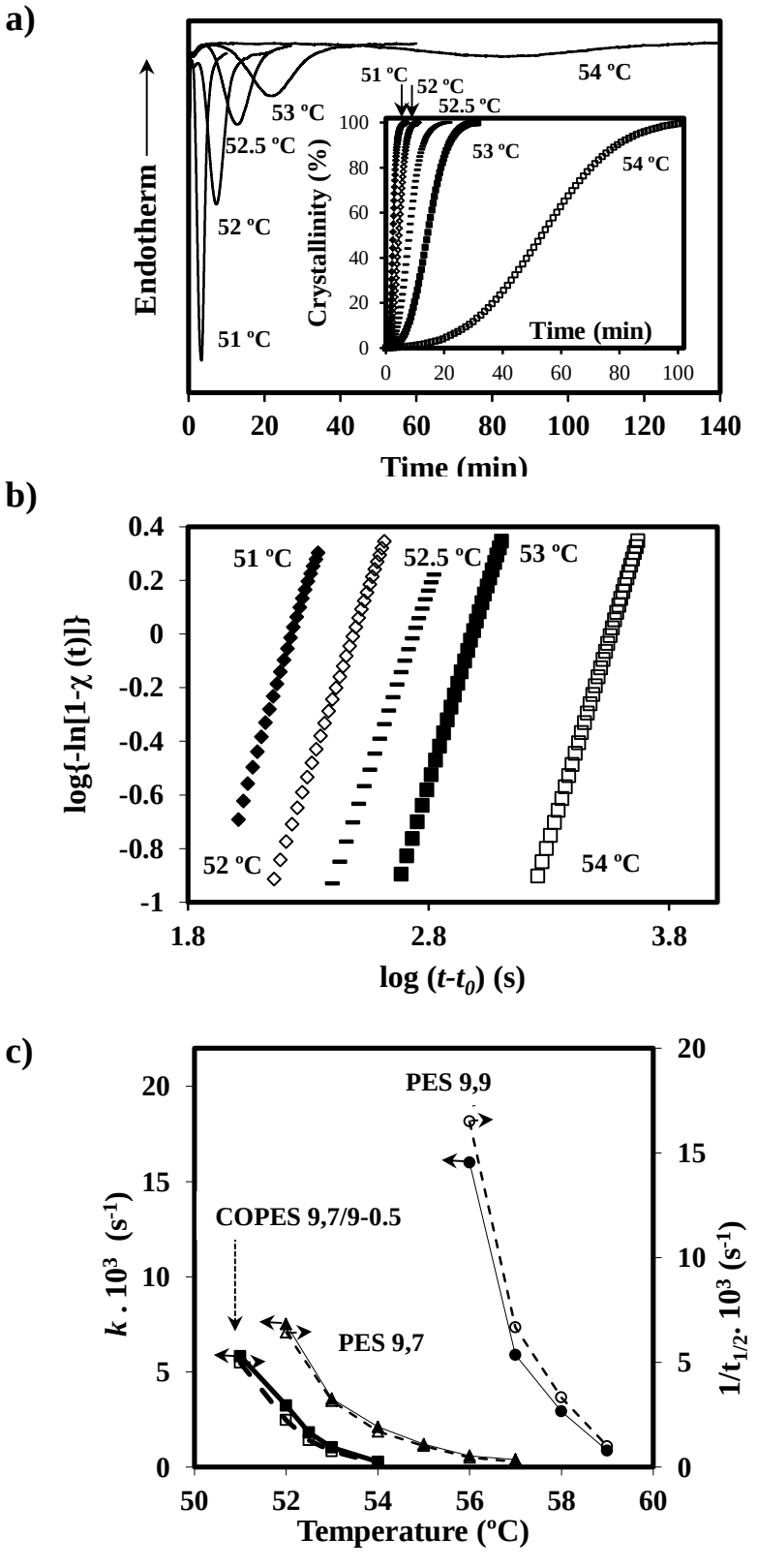

FIGURE 5

Díaz *et al.*

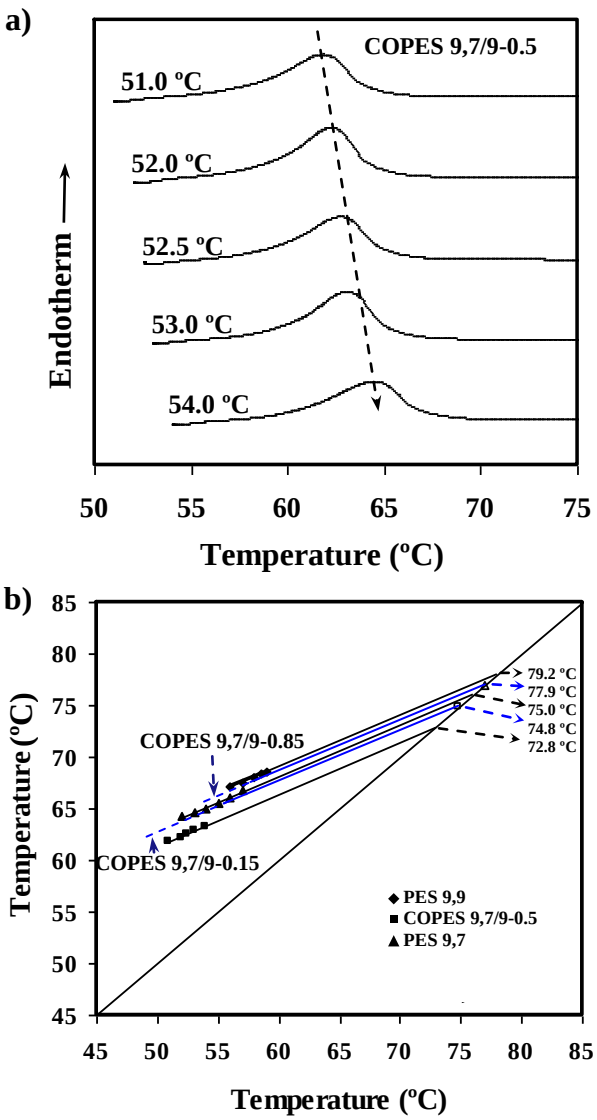

FIGURE 6

Díaz *et al.*

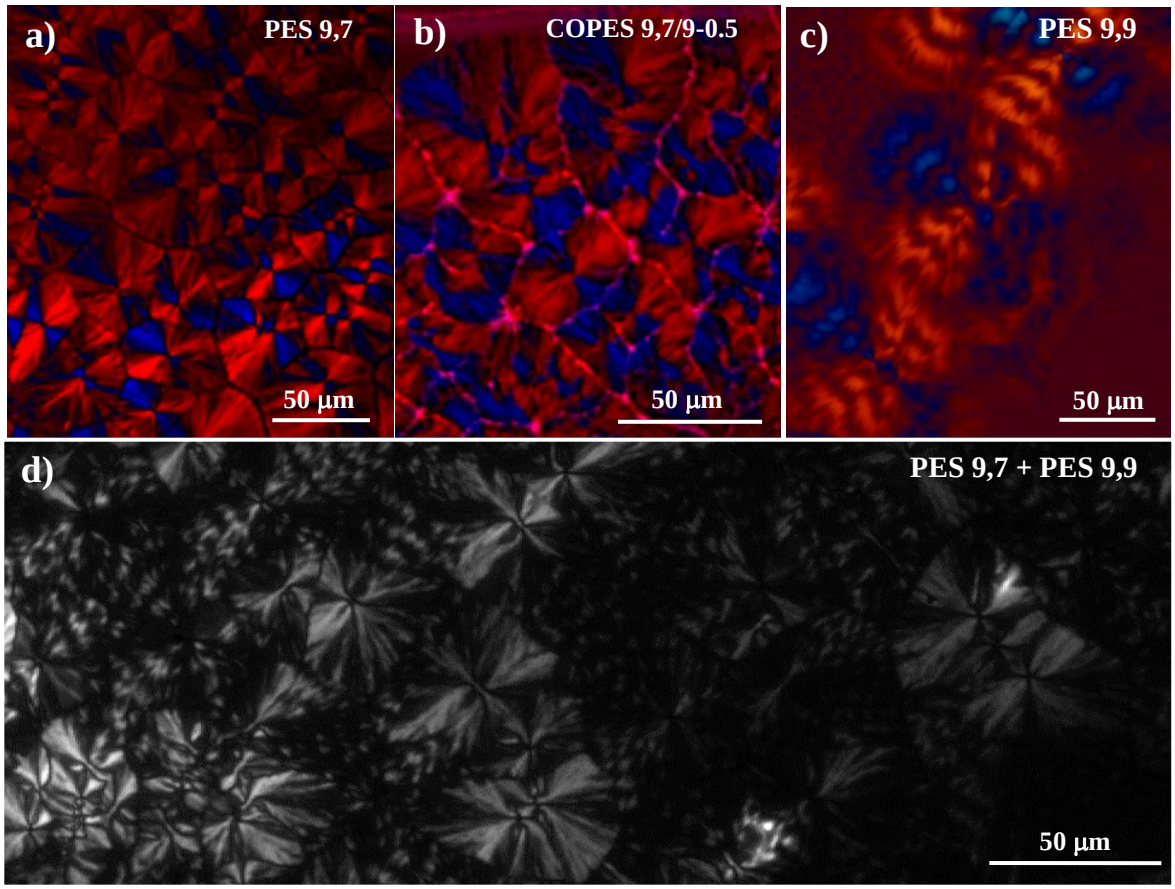

FIGURE 7

Díaz *et al.*

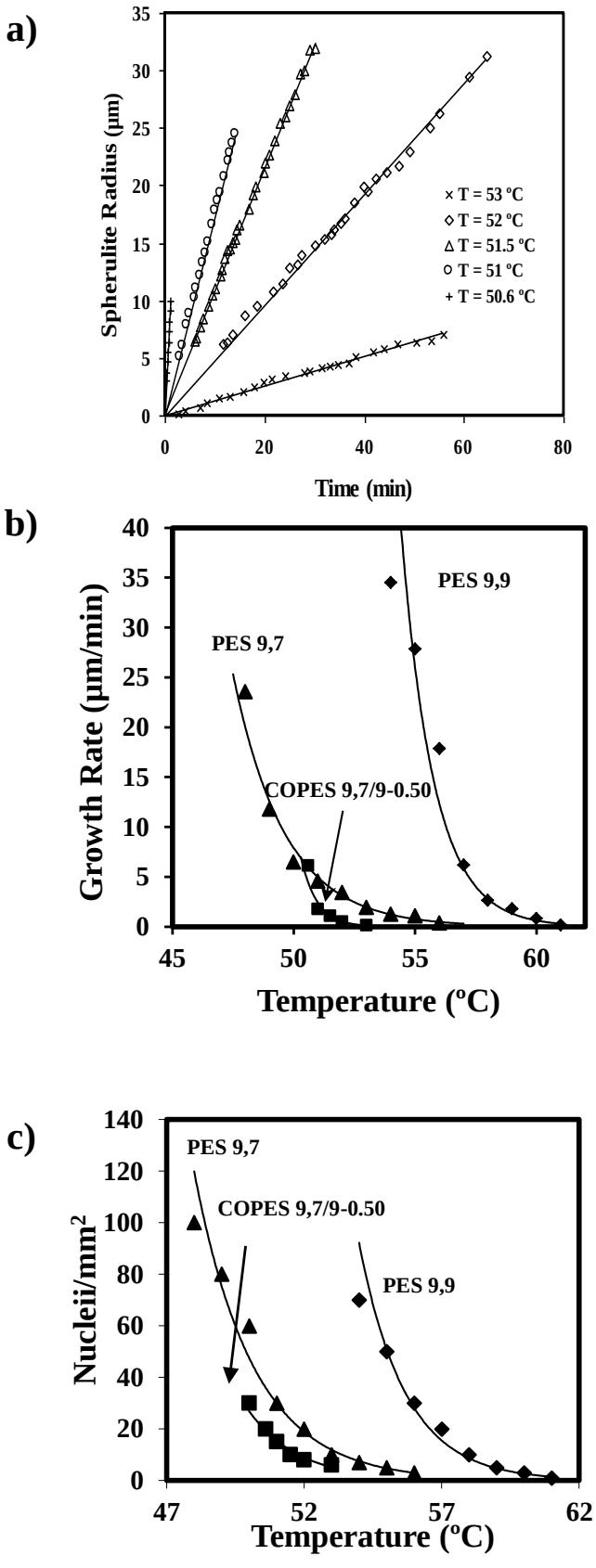

FIGURE 8

Díaz *et al.*

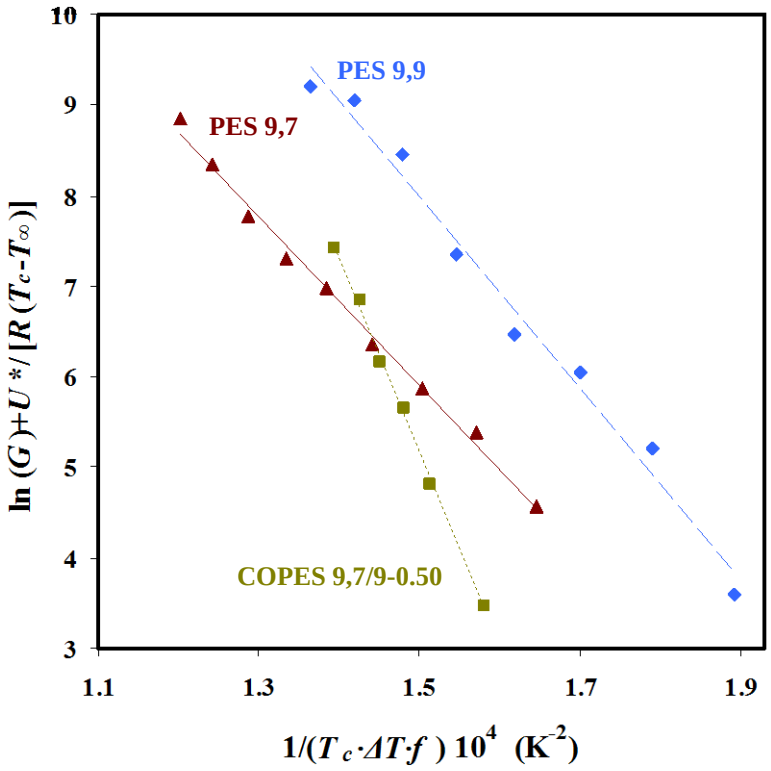

FIGURE 9

Díaz *et al.*

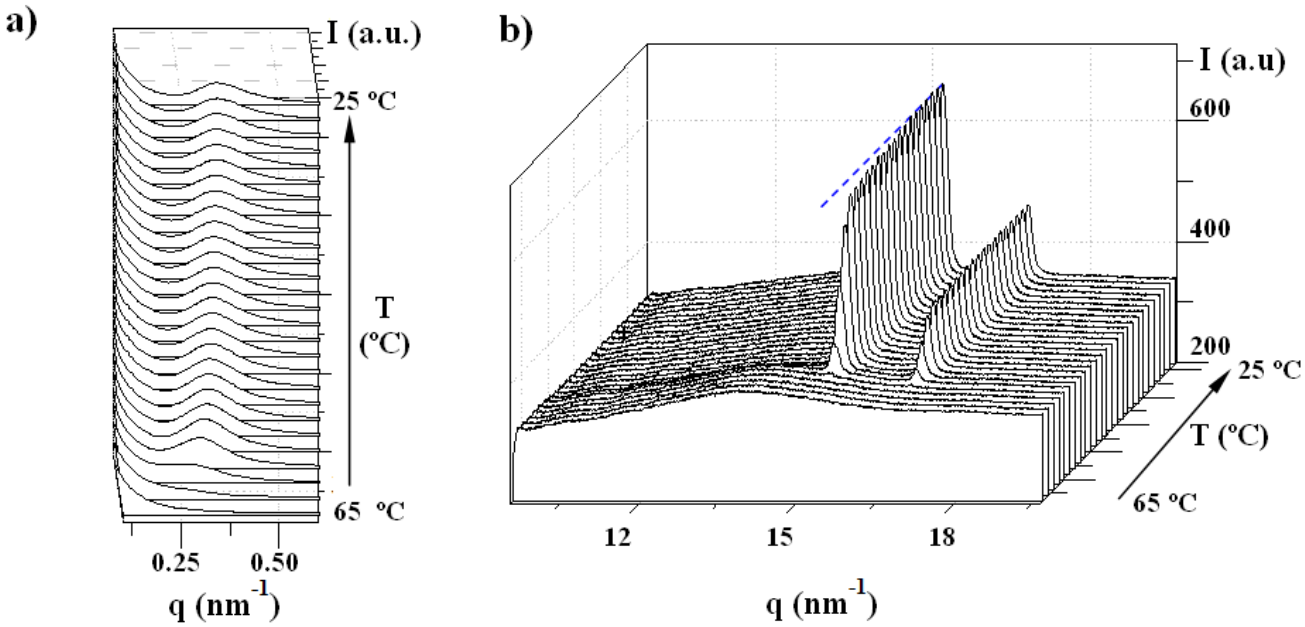

FIGURE 10

Díaz *et al.*

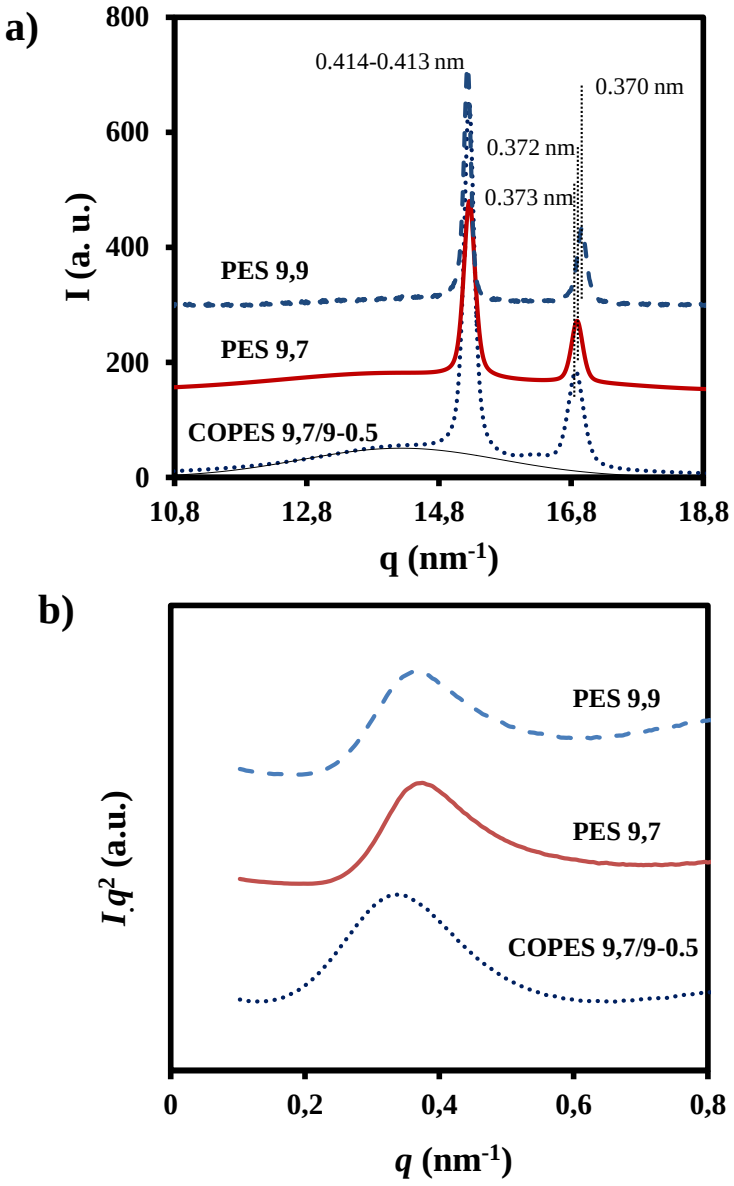

FIGURE 11

Díaz *et al.*

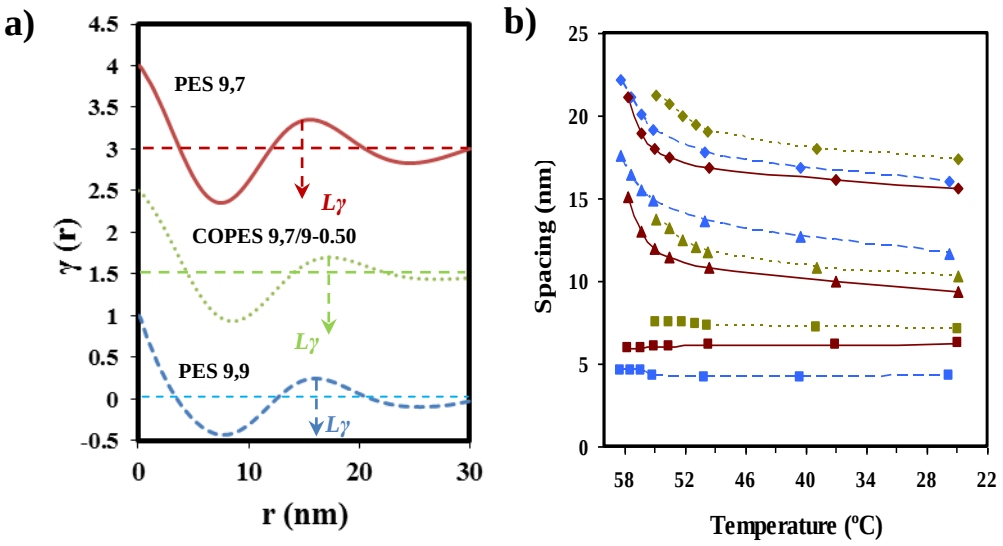

FIGURE 12

Díaz *et al.*